LiftWEC

DEVELOPMENT OF A NEW CLASS OF WAVE ENERGY CONVERTER BASED ON HYDRODYNAMIC LIFT FORCES

Deliverable D6.3
Structural Dynamic Model Development

Document Information

Project Acronym	LiftWEC
Project Title	Development of a new class of wave energy converter based on hydrodynamic lift forces
Grant Agreement Number	851885
Work Package	WP6
Related Task(s)	T6.3
Deliverable Number	D6.3
Deliverable Name	Structural Dynamic Model Development
Due Date	30th November 2021
Date Delivered	30th November 2021
Primary Author(s)	Abel Arredondo-Galeana (AAG)
Co-Author(s)	Weichao Shi (WS), Feargal Brennan (FB)
Document Number	LW-D06-03

Version Control

Revision	Date	Description	Prepared By	Checked By
1.0	15/10/2021	Internal working draft	AAG	WS, FB
1.1	03/11/2021	Internal draft for review	AAG	WS, FB
1.3	22/11/2021	Draft for consortium Review	AAG	WS, FB
2.0	30/11/2021	Submission to EU	AAG	WS, FB

EXECUTIVE SUMMARY

This document constitutes Deliverable '*D6.3 Structural Dynamic Model Development"* of the LiftWEC project. LiftWEC is a collaborative research project funded by the European Union's Horizon 2020 Research and Innovation Programme under Grant Agreement No 851885. It is the intention of the project consortium that the LiftWEC project culminates in the development of one or more promising configurations of a Wave Energy Converter operating through the use of one or more rotating hydrofoils that generate lift as the primary interaction with the incident waves.

In this report, a structural dynamic model is developed for LiftWEC to understand structural conditions that could amplify motions on the sub-structures and to evaluate the impact of these motions in the power performance of the device. To perform the analysis, LiftWEC is sub-divided into three sub-structures: the hydrofoils, the central shaft and the support structure. The support structure is modelled as a bottom mounted v-frame and each of the substructures is analysed individually and collectively.

The structure of deliverable is described briefly as follows. Firstly, the model is presented, and the corresponding equations of motion are introduced for each of the sub-structures, assuming two-dimensional flow. A separate single degree of freedom (DOF) is considered for the hydrofoils and the central shaft, namely with radial and rotational motion, respectively. Whilst a v-frame type of support structure with two DOFs (heave and surge) is considered. Secondly, the equations of motions are solved with a 4th order numerical integration scheme (Runge-Kutta) and the amplitude of the motions are obtained. Thirdly, instantaneous and some instances of frequency analysis are evaluated in order to obtain the relevant conclusions.

We note that in this analysis, the radial forces on the hydrofoils are the major drivers on the induced motions of the hydrofoils and support structure, whilst the tangential forces exert the highest influence in the central shaft. As such, the analytical tools provided by the consortium to model the loads on LifWEC have been utilised.

In this deliverable, it is found that passive control strategies, such as passive compliance can promote conditions that enhance the performance of the rotors. In particular, simple compliance of one of the foils seems to be beneficial in terms of power extraction. In contrast, it is found that compliance of the structure is not detrimental to the power output of the device.

TABLE OF CONTENTS

1   INTRODUCTION

This document constitutes Deliverable '*D6.3 Structural Dynamic Model Development"* of the LiftWEC project. LiftWEC is a collaborative research project funded by the European Union's Horizon 2020 Research and Innovation Programme under Grant Agreement No 851885.

1.1   PROJECT OUTLINE

The LiftWEC project focuses on the development of a novel type of Wave Energy Converter (WEC), called LiftWEC, which is intended to utilise hydrodynamic lift forces to incite device motion and extract wave energy using a rotating hydrofoil, as opposed to the more traditional approach of exploiting buoyancy and diffraction force regimes. This radically different approach to the design of wave energy converters offers the opportunity of making a step-change in the potential of wave energy, and thus lead the way for its commercialisation, where no commercially viable wave energy system currently exists.

1.2   PURPOSE OF DELIVERABLE

The primary purpose of this document is to identify the conditions that can prompt motion on the sub-structures of LiftWEC. Secondly, we aim to identify whether any of the induced motions could be beneficial in terms of power extraction. By dividing LiftWEC into three sub-structures 1) hydrofoils, 2) central shaft and 3) support structure, we present the equations of motion of each sub-system and excite each subsystem with the corresponding hydrodynamic loads. The range of motions of each sub-system is discussed and relevant conclusion are drawn in terms of feasibility and impact on power extraction.

1.3   STRUCTURE OF THE DOCUMENT

The structure of this document is as follows. First, we provide an overview to the structural dynamic model. We describe briefly LiftWEC, the rotor parameters, the hydrodynamic model main framework and the relevant wave conditions for the rotor. Then, we present the structural dynamic model, where we introduce the substructures, the corresponding equations of motion and the hydrodynamic loads that will be used to excite the systems. Subsequently we present three subsections, where results for the foil, central shaft and support structure system are discussed. Lastly, the relevant conclusions are presented. Three appendices are included, 1) validation of the hydrodynamic model, 2) one example of state-space notation of the structural dynamic model and 3) a summary of the Lagrange equations, which are used to obtain the equations of motion of each sub-system. We note that the systems of LiftWEC, are modelled through typical 1-DOF and 2-DOF systems, as such, literature examples can be found where the equations of motion are derived [1].

2 PREAMBLE TO STRUCTURAL DYNAMIC MODEL

2.1 THE LIFTWEC CONCEPT

The LiftWEC concept is shown in Figure 1. In this case, the rotor consists of two hydrofoils connected to a central shaft by radial spokes. The support structure, for the purposes of this study, is assumed to consist of two v-frames that are connected to the central shaft by means of roller bearings. The hydrofoils, of uniform cross-section along the span (S), rotate following the wave orbital motion. The phase of the rotation is controlled so that it is different to that of the incoming wave. This phase difference ($\Delta\varphi$) generates an inflow velocity w at an angle of attack α and hence a lift force in the hydrofoils. Provided that α does not exceed the stall angle of the hydrofoils, the tangential component of the lift force sustains the rotational motion of the device.

We note that this configuration is superficially different to the four configurations selected in *Deliverable D2.8 Specification of Baseline Configurations*, which narrowed down the range of LiftWEC support structures to a monopile, a semi-sub, a spar buoy and a TLP type of support structure. However, we recall that the hydrodynamics of the rotor (foil and central shaft) are similar for all of the configurations. Hence, results of the modules presented in this deliverable will be valid for all of the selected baseline configurations. Regarding the support structure, although the one shown in Figure 1 is different to those specified on *Deliverable D2.8 Specification of Baseline Configuration*s, we note that this deliverable will assess the potential effect of compliance of the structure. As such, the results presented here will still be relevant to any other configuration.
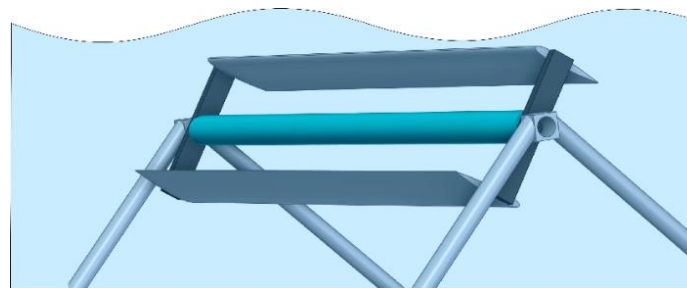

Figure 1 LiftWEC rotor aligned parallel to wave crest, showing the hydrofoils, the central shaft and the v-frame support structure

2.2 ROTOR PARAMETERS

It is important to specify the operational and structural parameters of LiftWEC used in the structural dynamic model. We identify the following parameters of importance: Rotor radius (r), submergence (μ), chord length (c), span (s), angular frequency (ω), phase difference ($\Delta\varphi$), mass of hydrofoil (kg), significant wave height (H_s) and peak period (T_p). The values utilised in this deliverable for each of these parameters are provided below in Table 1.

Parameter	Modelled value
Rotor radius (r)	6 m
Submergence (μ)	-12 m
Chord length (c)	4 m
Span (s)	10 m
Angular frequency (ω)	0.6283 rad/s
Phase difference ($\Delta\varphi$)	Hydrofoil 1: +90°, Hydrofoil 2: -90°
Mass of hydrofoil (kg)	15 tonnes
Significant wave height (H_s)	3 m
Peak period (T_p)	10 s

Table 1 Relevant operational and structural parameters of rotor

2.3 THE HYDRODYNAMIC MODEL

In order to carry-out a structural dynamics analysis, a hydrodynamic model is needed to model the loads on the hydrofoils and the structures of LiftWEC. The model used is based in two-dimensional flow assumptions and the main features are explained in Arredondo-Galeana et al. [2] published at the European Wave and Tidal Energy Conference (EWTEC 2021) [2]. The model was validated, for the case of constant angular velocity versus results from Scharmann [3] and the validation is included in Appendix 1. The model utilises two hydrofoils and the schematic representing the forces on the hydrofoils are depicted in Figure 2. We note that expansions of the model include the point-vortex model developed by Wehausen and Latoine [4], used by Siegel et al. [5], and implemented recently with the Dawson function by Emarkov and Ringowood [6]. These expanded models account for the induced velocities that a neighbouring foil imposes on a foil, and the induced velocity due to the wake of each foil. In the analysis carried out on this work, the flow field is modelled through the interaction of the rotor velocity and wave velocity only (see Figure 2). For the wave conditions tested in this deliverable, force results remain within 10% when compared to the results of the expanded models. As such, our analysis will provide a satisfactory insight into the structural dynamics of LiftWEC.
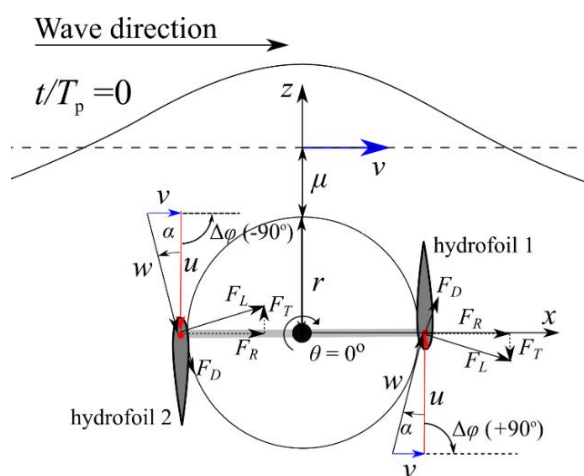

Figure 2 LiftWEC schematic showing two hydrofoils under wave-crest, rotating at a phase difference of $\Delta\varphi = 90°$

2.4   WAVE CONDITIONS

According to the Grant Agreement No 851885, the basis of design is associated with the large-scale production of energy for the European market using the North Atlantic wave climate. Hence, for the present analysis, we consider a Jonswap wave spectrum with a peak wave period (T_p) of 10 s and a significant wave height (H_s) of 3 m.

We put these figures into perspective in Figure 3. The figure shows the scatter plot data corresponding to a point in the North Atlantic at the coast of France, located at 47.84° N, 4.83° W. The figure shows the energy period (T_e) along the horizontal axis and H_s along the vertical axis. The data is available from the Ifremer FTP server and contains directional spectral wave data for 10-years between 2000-2010 [7] .

We note that we need to convert T_p to T_e to identify the wave testing conditions of Table 1 in Figure 3.The conversion is performed through $T_e = \alpha\, T_p$, where $\alpha = 0.9$ for a Jonswap wave spectrum [8] and the wave testing conditions are plotted with a red marker in the figure.

For this study, the selected wave parameters are $T_p = 10\ s$ and $H_S = 3\ m$ are those studied by Scharmann [3]. Hence the results presented on this deliverable consider representative sea state conditions that could be encountered off the coast of France.
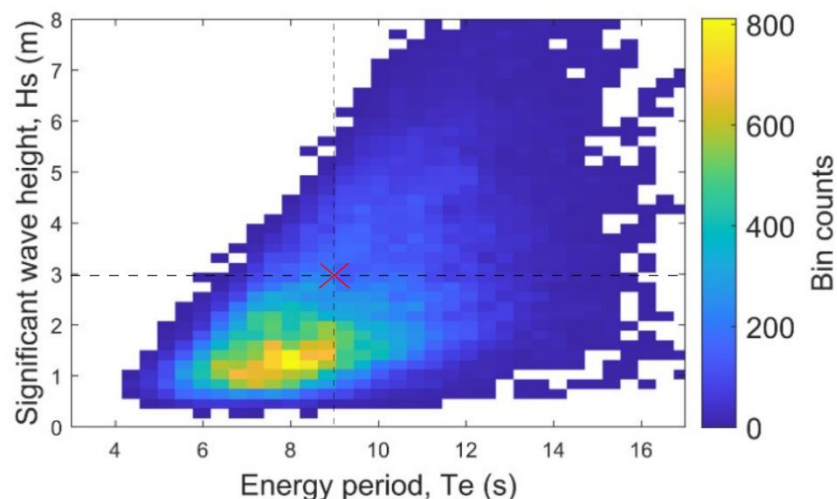

Figure 3 Energy period (T_e) versus significant wave height (H_s) from Homere database, for a location from the North Atlantic coast of France close to Quimper at 47.84° N, 4.83° W.

3 STRUCTURAL DYNAMICS MODEL

In this section, we introduce the structural dynamics model. We present first the subcomponents, the equations of motion and then the procedure to solve the equations. Finally, we present the time series of the hydrodynamic loads that is used to excite the subsystems of the model.

3.1 SUB-COMPONENTS FOR STRUCTURAL DYNAMIC MODELLING

The LiftWEC structure is subdivided into three sub-structures to carry out the structural dynamic analysis:

1. The hydrofoils.
2. The central shaft.
3. The support structure.

The hydrofoils and the central shaft are defined with 1-DOF each, with radial and rotational motion, respectively. Whilst the support structure is defined with 2-DOF, with motions in the horizontal and vertical axis. We summarise the sub-components, the corresponding equations of motion and the schematic of each sub-component in

Table 2. The equations of motion are derived or adapted from the literature [1, 9, 10] to the context of LiftWEC, and coupled to the hydrodynamic model. We note that the hydrodynamic model considers linear wave theory with two-dimensional flow assumptions, and it can be accessed in Arredondo-Galeana et al. [2], and with the point source expansion in Emarkov and Ringwood [6].
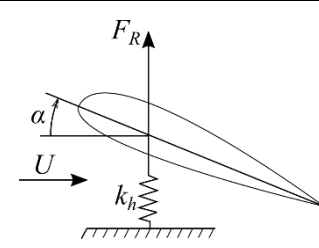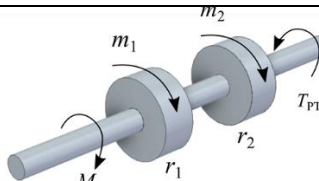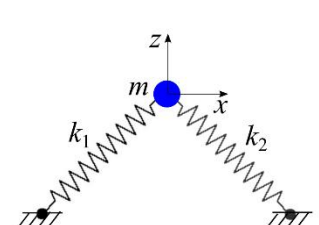
Subsystem	DOF	Equation		Schematic
Foil	Radial (h)	$m\ddot{h} + k_h h = F_R$	(1)	
Central shaft	Rotation (θ)	$I\ddot{\theta} = M - T_{PTO}$	(2)	
Support structure	Horizontal displacement (x) Vertical displacement (z)	$m\ddot{x} = (\sum F_x + \vec{F}_1 + \vec{F}_2) \cdot \hat{e}_1$ $m\ddot{z} = (\sum F_z + \vec{F}_1 + \vec{F}_2) \cdot \hat{e}_2$	(3) (4)	

Table 2 Summary of LiftWEC sub-components modelled in the structural dynamics model, with corresponding equations of motion and schematic of sub-system

In equation 1, m is the mass of the hydrofoil, h is the radial motion, $\ddot{h}$ is the radial acceleration, k_h is the linear stiffness coefficient of the spoke holding the hydrofoil and F_R is the radial force acting on the hydrofoil. Whilst, in equation 2, I is the inertia of the rotor, $\ddot{\theta}$ is the angular acceleration, M is the moment acting on the shaft and T_{PTO} is the torque applied to the shaft by means of a power-take off mechanism. We note that M is the moment due to the tangential force on the hydrofoils, and that the rotation of the motor could be controlled by means of torque T_{PTO} or by means of angular velocity $\dot{\theta}$ and acceleration $\ddot{\theta}$.

Finally, equations 3 and 4, are the corresponding equations of a non-linear 2-DOF system, where the horizontal and the vertical displacements are x and z, respectively, m is the mass of the support structure and k is the structural stiffness of the support. We note that support structure is a v-frame, hence the springs represented in the schematic of Table 2 Summary of LiftWEC sub-components modelled in the structural dynamics model, with corresponding are virtual springs whose stiffness is estimated based on the stiffness of the v-frame support structure. These assumptions will also be elaborated in Sec 4.

3.2   PROCEDURE TO SOLVE EQUATIONS OF MOTION

In this section, the procedure to solve the equations of motion presented in Table 2 is explained. In general, the equations of motion are weakly coupled to the hydrodynamic model, following the procedure suggested in Ramesh et. al. [9]. Ramesh et al. use an Adam-Bashforth integration scheme, here we utilise a Runge-Kutta 4th order integration scheme for faster convergence.

The steps to solve the equations of motion are as follows:

1) Hydrodynamic loads ($F_R, M, \sum F_x \ and \ \sum F_z$) are computed with the numerical model of LiftWEC at time step n.

2) The computed loads are coupled to the equations of motion (Eqs. 1, 2, 3 and 4).

3) The structural states are solved through integration schemes (Runge-Kutta 4th order) and determined at time step n+1

4) Procedure is repeated from step 1, for time step $n + 1$

Further details are found in Appendix 2, where the procedure to solve Equation 1 in state-space notation is presented. State-space notation is a useful representation to code the solution for this type of problem.

3.3   SHAPE OF HYDRODYNAMIC LOADING

The shape of the loads that LiftWEC experiences are presented in this section to understand the type of motion that could be encountered by the substructures of LiftWEC. For simplicity, the point vortex and wake radiation component are disabled on the codes and only the velocity due to the wave and the rotation of the rotor are considered in the figures below. In fact, changes in forces due to the point

vortex and wake radiation terms remain below 10% with the parameters tested in Table 1. As such, the simplified version of the model is accurate to provide insight into the dynamics of LiftWEC. Figure 4a and Figure 4b show the radial and the tangential forces on two hydrofoils (blue represents hydrofoil 1 and red represents hydrofoil 2) at constant angular velocity. The radial forces determine the radial motion of the foils and of the support structure, whilst the tangential forces determine the behaviour of the central shaft. It is noted in Figure 4a, that one of the foils is in tension whilst the other one is in compression due to the opposite sign in radial forces, whilst Figure 4b shows that the tangential forces act on the same direction in both hydrofoils and that they are oscillating in nature.
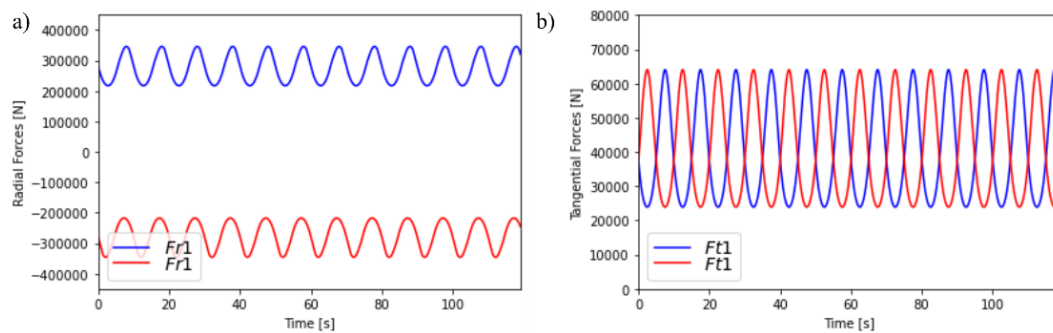

Figure 4 a) Radial and b) tangential forces on hydrofoil 1 (in blue) and 2 (in red) for a regular wave case with Tp = 10 s, Hs = 3 m with constant angular velocity and a phase difference of 90 degrees

Incorporating inertia, results are presented in Figure 5a and Figure 5b. We note, that the radial forces have a similar trend to the case of constant angular velocity, i.e. one foil is in tension and one in compression. The tangential forces also have a similar pattern to the case of constant angular velocity. Hence, as expected, the compliance of the foils has the same effect as those presented in the previous section without inertia. In the subsequent sections, we validate this hypothesis. We note that when inertia is considered, the rotation frequency of the rotor is capped at the angular frequency of the incoming wave in order to produce power.
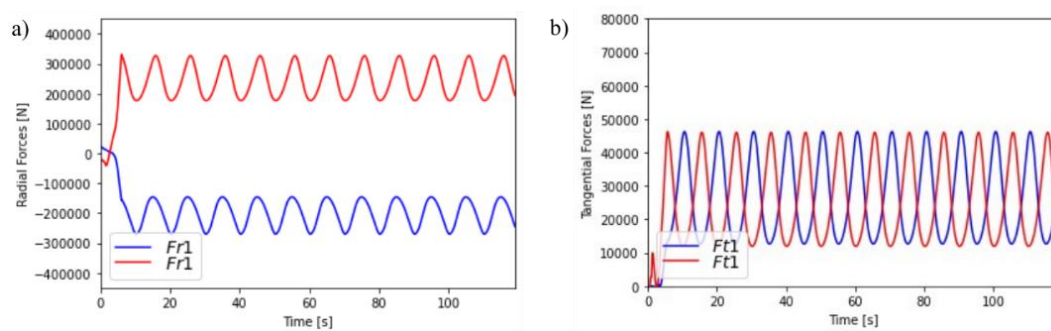

Figure 5 a) Radial and b) tangential forces on hydrofoil 1 (in blue) and 2 (in red) for a regular wave case with Tp = 10 s, Hs = 3 m with inertia and a phase difference of 90 degrees

In remaining analysis, we consider the action of the radial forces in the hydrofoils and support structure. For both substructures, we consider constant angular velocity. For the central shaft, we will consider the tangential forces and inertia. This is performed to account for the forces generated due to changes in angular velocity.

4 HYDROFOIL STRUCTURAL DYNAMICS

Structural nonlinearities in hydrofoils can occur due to large deformations, material properties or loose linkages [10], whilst hydrodynamic nonlinearities can occur due to viscous effects. In particular, at low Reynolds numbers, such as those tested in laboratory settings, and low reduced frequencies, leading-edge vortices and resulting dynamic stall could result in violent vibrations and induce failures [9]. In contrast, at high Reynolds numbers, such as in large-scale devices, these effects might become less dominant and only wave and structure interactions might become relevant.

In this report, we will consider the case of attached flow conditions, and structural non-linearities that arise due to material stiffness and wave interactions. Attached flow conditions can be promoted by minimising the amplitude in the angle of attack oscillations of the hydrofoils, for example, by controlling the rotational speed of the rotor. This can increase the magnitude of the tangential velocity component on the foil and therefore, reduce the angle of attack on the foil.

The method used to model the fluid structure interaction model is implemented numerically in Python. This enables a parametric analysis of different stiffnesses, and different wave and rotor parameters in an efficient and inexpensive computational manner. The hydrodynamic load validation of the code has been performed versus forced wave cycloidal converter data from Scharmann [3] and it is included in Appendix 1.

4.1 HYDROFOIL EQUATIONS OF MOTION

Figure 6 shows a 1-DOF system of a hydrofoil following the model of Ramesh et al. [9], in radial motion. In the figure, the radial motion is coupled to a compressional spring. The stiffness of the radial spring (k_h) corresponds to the longitudinal stiffness of the strut that connects the central shaft to the hydrofoil. In the figure, the spring represents this connecting strut. The radial force (F_R) excites and drives the motion of the system.
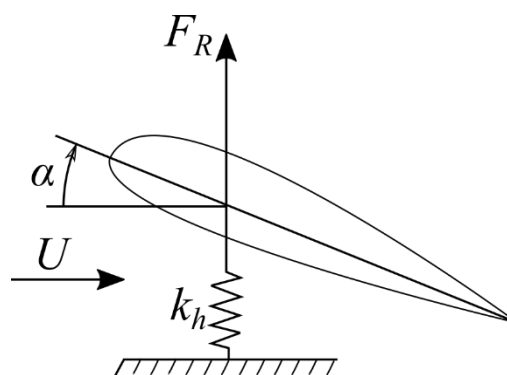

Figure 6 1DOF system for LiftWEC hydrofoil adapted from Ramesh et al. [1]

The mass of the hydrofoil is 15 tonnes. We considered steel with a density of 8050 kg/m³, with a chord $c = 4$ m and a span $s = 10$ m. We recall that the hydrofoil is not solid and only a fraction of the solid volume equal to 0.1 is considered to compute its mass. It is worth noting that in Figure 6, the foil is neutrally buoyant. We recall that the equation of motion for radial motion is

$$m\ddot{h} + k_h h = F_R$$

where m is the mass of the hydrofoil, k_h is the radial spring stiffness, h is the radial motion, $\ddot{h}$ is the radial acceleration, F_R is the radial force on the foil.

4.2 FREE RADIAL OSCILLATION

The motion of the hydrofoils is studied under free oscillation. Although the hydrofoils will experience a force when the rotor is in operation, a free oscillation test is useful to understand the basic structural dynamics of the system. Therefore, the two hydrofoils are displaced 1 m and are left to oscillate without any external forces being applied. The simulation parameters are provided in Table 1.

The direction of the displacement is opposite in both hydrofoils to be consistent with the direction of the forces during operation, i. e. one hydrofoil is under tension, whilst the other is under compression, as shown with the radial forces of Figure 4 and Figure 5. A low stiffness case and a high stiffness case are assessed to observe the effect of stiffness of the strut supporting the hydrofoils. In this example, low stiffness is defined as $k_h = 500\ kN/m$ and high as $k_h = 2000\ kN/m$. We note that the low stiffness case, could be physically unrealistic if the support of the hydrofoil is made of steel, but it is useful to illustrate the effects of very low stiffness on the dynamics of the system.

Results are shown in Figure 7. Figure 7a shows the low stiffness case, whilst Figure 7Figure 7b shows the high stiffness case. The top row of the figure shows the radii of the two hydrofoils, whist the bottom row shows the power of the rotor. Results show that increasing the stiffness increases the frequency of oscillation the system, whilst the mean power output remains constant and independent of the stiffness.
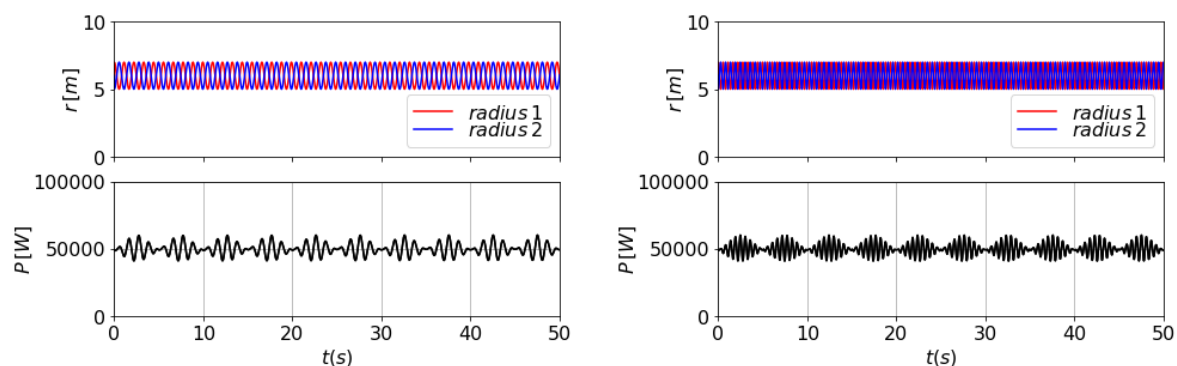

Figure 7 a) Low stiffness case under free oscillation and b) high stiffness case under free oscillation

The effect of stiffness on the angular natural frequency of the system ω can be explained through

$$\omega = \sqrt{\frac{k}{m}},$$

where k is the stiffness of the system and m is the mass of the hydrofoil. Increasing the mass of the hydrofoil has an inverse effect and reduces the natural frequency of the system. Hence, m can also be utilised to tune the dynamics of LiftWEC and avoid resonant conditions with wave frequencies. We recall that $\omega = 2\pi f$, where f is the natural frequency.

4.3   FORCED RADIAL OSCILLATION

In this section the hydrofoil dynamic system is excited with the radial force (F_R) that occurs during operation, for the set of parameters specified in Table 1. First, results for very high stiffness (rigid system) are presented in Figure 8 Forced radial oscillation for high stiffness case. The first row shows the two radii of the two hydrofoils, which are overlapped because negligible deformation is present. The power output remains uniform. A constant rotational velocity of the rotor is $\omega = \frac{2\pi}{T_p}$ is utilised.
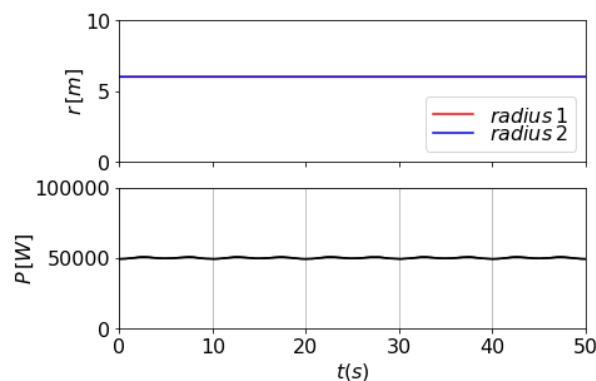

Figure 8 Forced radial oscillation for high stiffness case. The first row shows the two radii of the two hydrofoils, whilst the second row shows the power output

We now consider two scenarios of low stiffness. The first scenario is the single compliant case, where only one hydrofoil has low stiffness and the other one has high stiffness. The second scenario is the double compliant case, where both hydrofoils have low stiffness. Results are show in Figure 9a and Figure 9b, respectively. It can be seen that in the single compliant case, the hydrofoil with low stiffness is under tension and the oscillations have a higher amplitude that the average radius. In contrast the second hydrofoil remains at the average radius. In the double compliant case, both radii change, one remains above 6 m under tension, and the other one remains mostly below 6 m under compression. The single compliant case has a greater average output power as opposed to the double compliant case. This is because in the double compliant case, any gain in power from the hydrofoil in tension is cancelled out or mitigated by the second hydrofoil in compression.
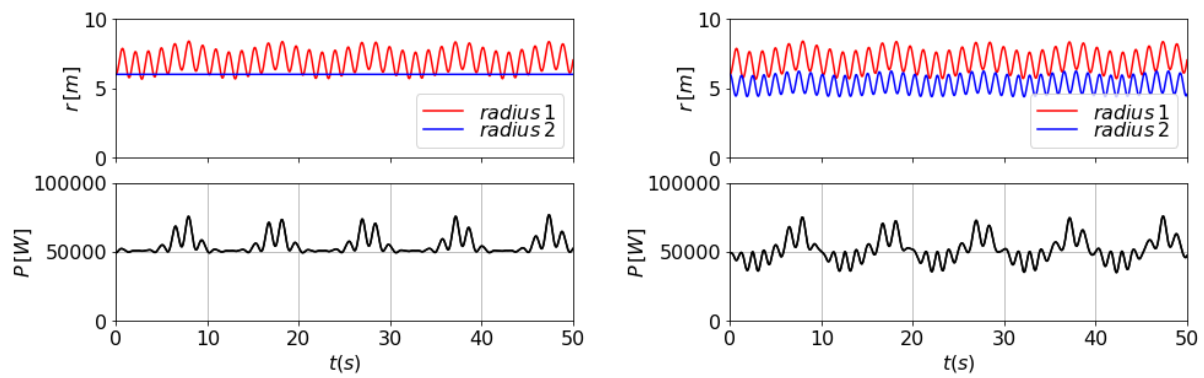
Figure 9 Radii and power output of a two-foil wave bladed cyclorotor with low radial stiffness for a) single compliant and b) double compliant system

4.4   STIFFNESS VERSUS MEAN OUTPUT POWER

We quantify the increase in mean output power due to different stiffness for the single compliant and the double compliant cases. The threshold limit for the lowest stiffness case is that where the radius reaches the through of the wave, i.e. for a submergence of 12 m (measured from mean sea level to the central shaft), a radius of 6 m and $H_s = 3$ m, a maximum deflection of 50% of the original radius is allowed. Results show that it is theoretically possible to obtain a gain in mean output power of about 10% for the single complaint case, for the lowest stiffness case. The gain in the double compliant case is reduced for all the tested cases, and a maximum gain of about 3% is reached for the lowest stiffness case.
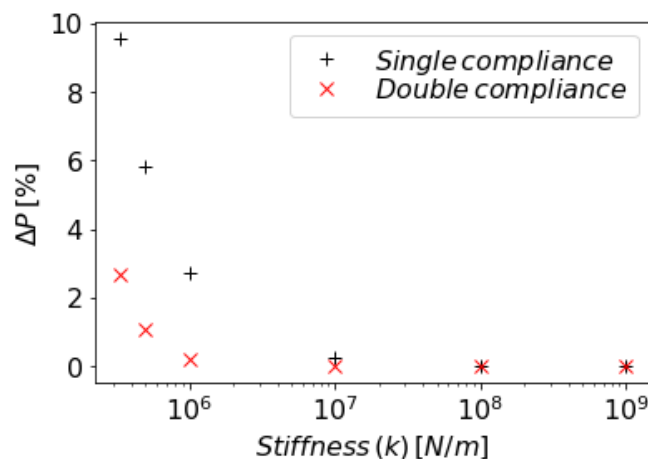

Figure 10 Stiffness versus change in mean output power for single and double compliant system

4.5 FREQUENCY ANALYSIS OF RADIAL SYSTEM

A power spectral analysis is carried out to observe the interaction between the excitation wave frequency and the hydrofoil radial frequency for the single compliant case. This approach allows us to identify scenarios that could approach resonance. If resonance occurs, then detuning of the system through variable mass or variable stiffness is recommended.

Figure 11a and Figure 11b the power spectrum density (PSD) of the radius and of the output power, respectively. Three different stiffnesses are studied and are labelled as low, medium and high. The corresponding stiffnesses values are $k_h = 333$ kN/m, , 1000 kN/m and 1,000,000 kN/m, respectively. Time series are simulated for a duration of $30T_p$, where T_p = 10 s. We recall that the purpose of this study is to understand resonant scenarios. Therefore, the signals are plotted with a vertical offset for ease of interpretation.

Results show a maximum first peak at $f = 0.1$ Hz in both figures. This corresponds to the peak wave frequency, which has peak wave period of $T_p = 10$ s. The second maximum peak is detected at the radial frequency and corresponds to the natural frequency of the radial system. For the low, medium and high stiffness cases, these peaks are located at 0.74, 1.28 and 40.48 Hz, respectively. These frequencies are highlighted with black dotted vertical lines in both figures. It is interesting to note that over a range of $6 \, s < T_p < 14 \, s$, which is a range that covers more than 80% of the wave data of Figure 3, resonance is not expected.

Among the tested cases, the high stiffness case could correspond to the properties of an existing material, whilst the low and medium stiffness cases would have to be implemented through springs. Hence, it is expected that resonance will not be an issue if the hydrofoil support struts are manufactured with offshore steel or any other material of high stiffness. Interestingly, there is room for single compliance to enhance the energy extraction of the system, whilst keeping the system safe and away from resonant behaviours.
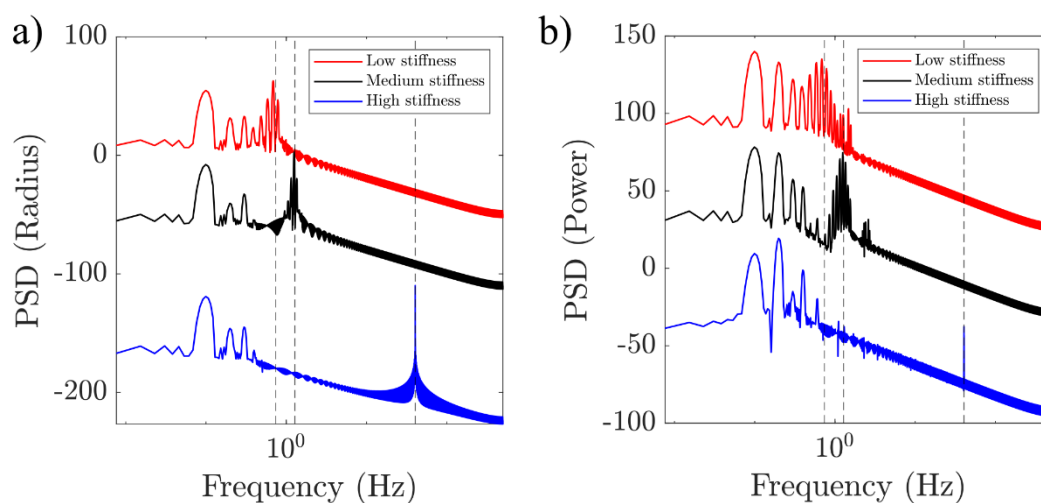

Figure 11 Power spectral density of a) radius and b) power for simply compliant system tested at low, medium and high stiffness

In order to estimate the stiffness of a rigid material, we compute the axial stiffness of the strut that supports the hydrofoil. From deliverable *D6.1 Extreme Event LiftWEC ULS Assessment* [11], the axial strut depicted in Figure 10 experiences tension under an axial load, in this case, the radial force F_R which is applied on the surface area A.
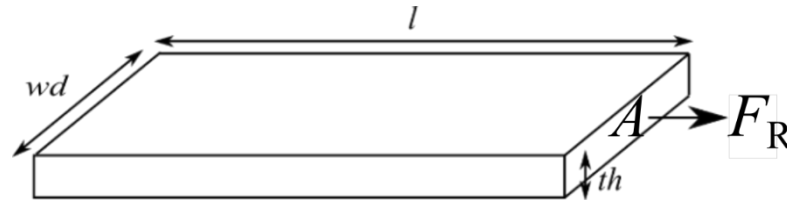

Figure 12 Lateral support of hydrofoil. Dimensions of the support are the length (l), thickness (th) and width (wd). In the figure, a force F applies tension or compression on the structure.

The axial stiffness (k_h) of the strut is computed with

$$k = \frac{EA}{l},$$

where *E* is the elastic modulus of the material, *A* is the cross-sectional area given by $wd \times th$ and *l* is the length of the strut or the radius of the rotor (r). We vary *A* between 0.1 m² to 1 m², and plot k_h for structural steel, aluminium alloy and ABS in solid, dotted and dashed dotted black lines. The elastic modulus for these materials is 210 GPa, 72.4 GPa and 2.4 GPa, respectively. The figure shows that the high stiffness case, with $k_h = 1,000,000$ kN/m, could be representative of an existing solid material, such as steel or an aluminium alloy. In contrast, the medium and low stiffnesses cases are too low to represent a commercial material. Hence, in order to achieve such stiffnesses, the compliance of the strut would need to be achieved passively by means of a spring or actively by means of a smart material of variable stiffness.
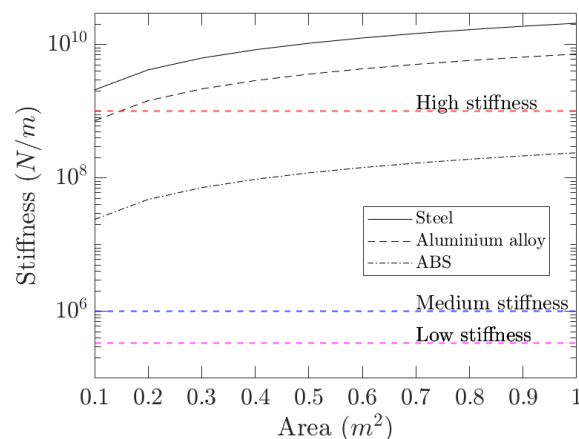

Figure 13 Stiffness versus surface area of strut for three different materials: structural steel, aluminium alloy, and ABS. Thresholds of high, medium and low stiffness are plotted with horizontal lines in the figure

5 ROTOR STRUCTURAL DYNAMICS

5.1 EQUATIONS OF MOTION

The equation of motion of the central shaft is defined as

$$I\ddot{\theta} = M - T_{PTO},$$

where I is the moment of inertia, $\ddot{\theta}$ is the angular acceleration of the rotor, M is the moment due to the tangential force on the hydrofoils and T_{PTO} is the torque applied to the PTO. The moment due to the tangential forces is defined as

$$M = [T_i r_i + T_j r_j],$$

where r and T are the radius and tangential forces of hydrofoil 1, denoted by subscript i and hydrofoil 2 is denoted by subscript j. The tangential forces can be computed as

$$T_i = \frac{1\rho U_i^2 bc}{2}[C_{L,i} \sin \alpha_i - C_{D,i} \cos \alpha_i] \qquad \text{and} \qquad T_j = \frac{1\rho U_j^2 bc}{2}[C_{L,j} \sin \alpha_j - C_{L,j} \cos \alpha_j]$$

where C_L and C_D are the lift and drag coefficients of the hydrofoils, ρ is the density of the fluid, b is the span of the hydrofoil, c is the chord length, α is the angle of attack of the hydrofoils.

For a system of two hydrofoils, the inertia of the rotor is

$$I = m_1 r_1^2 + m_2 r_2^2$$

where the m_1 and m_2 are the masses of hydrofoil 1 and hydrofoil 2, and r_1 and r_2 are the radii of the two hydrofoils. The system is shown in Figure 14 as a two-mass system (two hydrofoils) and two torques, M and T_{PTO}, which represent the hydrodynamic input and the control input, respectively.
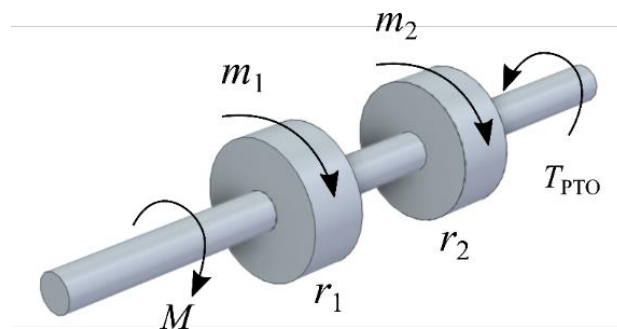

Figure 14 Two-mass dynamic system, representing the two foils of the system. The foils generate the hydrodynamic input (M) and an external control input (T_{PTO}) is applied to the shaft. The dynamics of the system are modelled with the equation of motion of the central shaft.

5.2 DYNAMIC RESPONSE OF CENTRAL SHAFT, WITHOUT PTO

Figures 15a and 15b show the radii of the hydrofoils and the angular velocity on the top row, and the power ouput on the bottom row, for a system with inertia for the cases of free rotation (ω_{free}), and capped angular velocity at wave frequency (ω_{x1}), respectively. The angular velocity of a system with inertia needs to be controlled once the velocity reaches that of the incoming wave. This is because if the system is not controlled and the angular velocity of the rotor is set free (ω_{free}), the average power production could tend to zero, as indicated by Figure 15. In contrast, if the system is controlled an the angular velocity is capped at the wave frequency ω_{x1}, then power production is positive. This an be observed in Figure 15b.
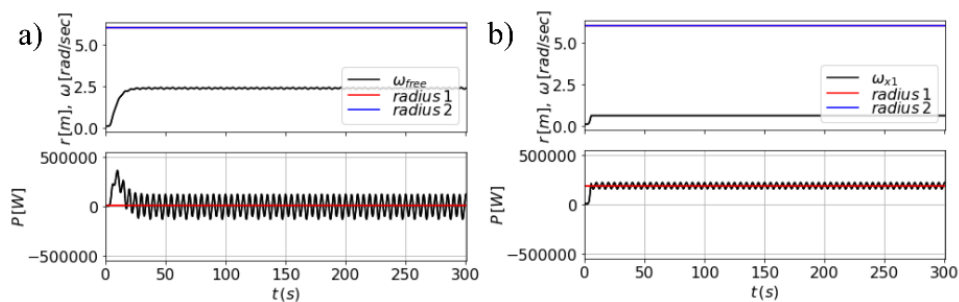

Figure 15 a) system with inertia without angular velocity control and b) system with inertia with angular velocity capped at the wave frequency (ω_{x1})

We incorporate the effect of compliance to the system, with single and double foil compliance in the results of Figure 16a and Figure 16b, respectively. A stiffness value of k_h = 2E6 N/m is utilised for this example. The radii oscillations can be seen in the top row of the figures, whilst the average power output is plotted in the bottom row of the figures. The test cases are presented for a duration of $30T_p$ as in the previous example. Results show that single compliance provides a slight advantage over no compliance, whilst double compliance does not seem to be beneficial in terms of average output power P_{av}. We investigate this further in the next section by testing a range of different stiffnesses and quantifying P_{av} for each case.
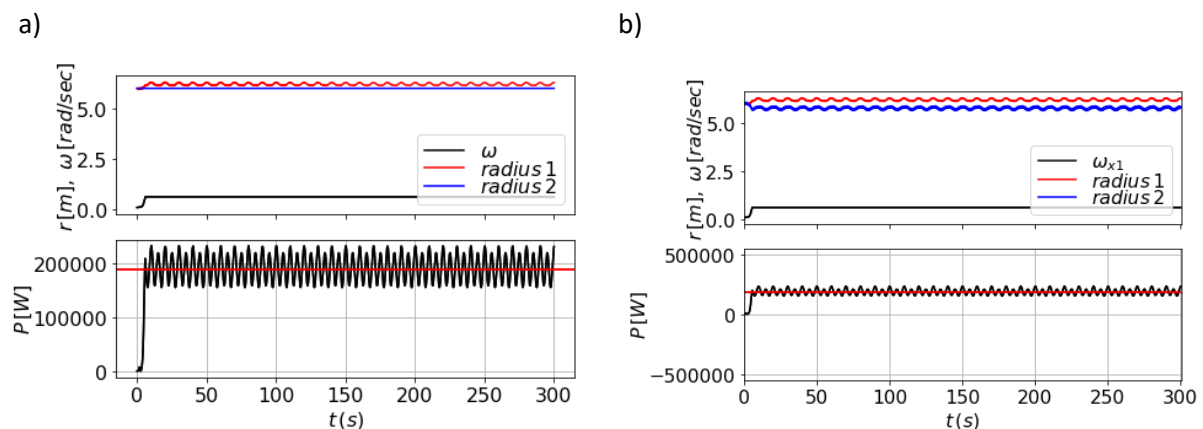

Figure 16 Structural response of central shaft without PTO for low stiffness with a) single compliance and b) double compliance. The stiffness of system is k_h = 2E6 N/m

5.3   MEAN OUTPUT POWER VERSUS DIFFERENT STIFFNESSES

The effect of variable stiffness is now explored in P_{av}. The stiffness is varied over a range of high stiffness to low stiffness as illustrated in Figure 13. A duration of $1000T_p$ is utilised to compute the steady state value of P_{av}. Different stiffnesses values are shown in Table 3 for the single and double compliant case. Results show that lower stiffness increases P_{av} for the single compliant case, whilst the gain in P_{av} for the double compliant case is minimal. These results are in agreement with those presented in Sec. 2.4 for a system operating at constant ω.

Table 3 Simply and doubly compliant average power output versus different stiffnesses for system with inertia. In the table Dt is the time step.

Stiffness	Simply compliant (P)	% change	Double compliant (P)	% change	Duration	Dt
1.00E+09	182962.8615	0.00%	182959.034	0%	1000Tp	0.01
1.00E+08	182991.2633	0.02%	182953.259	0%	1000Tp	0.01
1.00E+07	183277.1186	0.17%	182903.081	0%	1000Tp	0.01
5.00E+06	183599.5653	0.35%	183565.492	0%	1000Tp	0.01
3.33E+06	183923.6256	0.53%	183531.360	0%	1000Tp	0.01
1.00E+06	187784.1515	2.64%	184864.286	1%	1000Tp	0.01

5.4   CENTRAL SHAFT DYNAMICS WITH PTO

The effect of adding a PTO torque to the power production is shown in this section in Figure 17. We specify a PTO = $0.2T_{in}$. The effect of the power response of the system is to delay the ramp up to constant angular velocity to about $t = 6\ s$, as opposed to the case where no PTO is applied where the ramp time is about $t = 2\ s$ (Figure 16b).
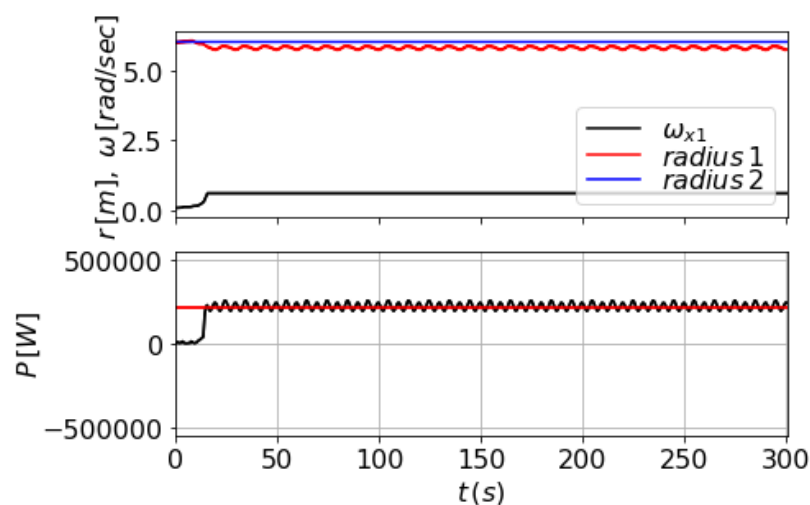

Figure 17 High stiffness case with a PTO opposing the torque generated by the tangential forces

6 FRAME STRUCTURAL DYNAMICS

The structural dynamics of a v-frame structure (Figure 18a) is modeled through a nonlinear 2-DOF system with two springs (Figure 18b). The springs are oriented along the legs of the support structure, as indicated in Figure 18b. The model can help in understanding the effect of compliance in the power output of LiftWEC. Furthermore, the model could allow for the evaluation of the dynamic behaviour of a monopile type of structure by considering only one spring oriented along the x- axis, as a structural or a soil type of spring [12].
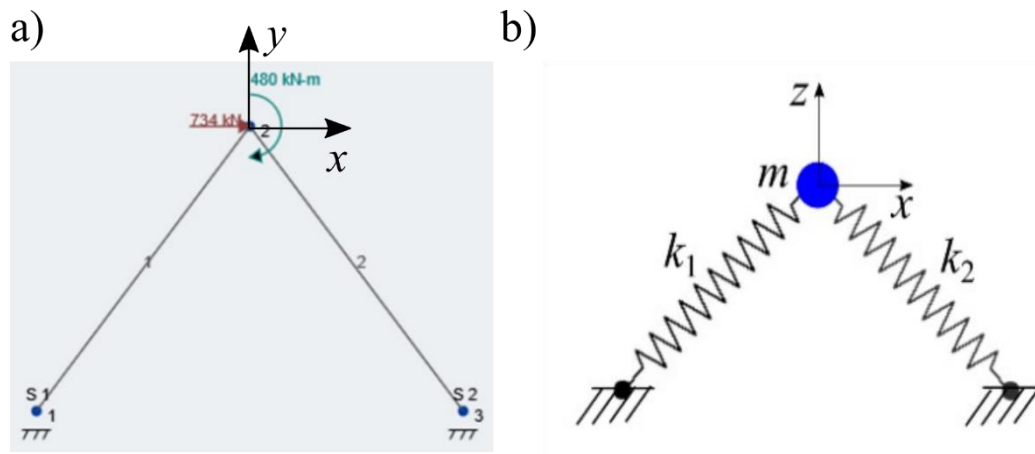

Figure 18 a) Simplified model of support structure and b) 2DOF non-linear system representative of support structure

6.1 EQUATIONS OF MOTION FOR 2-DOF NON-LINEAR OSCILLATORY SYSTEM

The system presented in Figure 18b, which represents the v-frame support structure of Figure 18a, can be modelled through the following equations of motion:

$$m\ddot{x} = (\sum F_x + \vec{F}_1 + \vec{F}_2) \cdot \hat{e}_1 \qquad \text{and}$$

$$m\ddot{z} = (\sum F_z + \vec{F}_1 + \vec{F}_2) \cdot \hat{e}_2$$

where m is the mass of the rotor, $\vec{F}_1$ and $\vec{F}_2$ are the restoring forces acting on the springs due to their deformation, $\sum F_x$ and $\sum F_z$ are the excitation forces along the x and z-axes, and $\hat{e}_1$, and $\hat{e}_2$ are the unit vectors oriented along the x and z-axes. As a reference, the derivation of the equations of motion of similar systems can be found for example in S. Rao S. , 2010 [1] or in the github repository of Andrew Friedman [13]. $\vec{F}_1$ and $\vec{F}_2$ are defined as:

$$\vec{F}_1 = k_1\Delta_1\hat{e}_{r_1} \text{ and}$$

$$\vec{F}_2 = k_1\Delta_2\hat{e}_{r_2},$$

where k_1 and k_2 are the stiffnesses of spring 1 and spring 2, Δ_1 and Δ_2 are the change in length of the springs, $\hat{e}_{r_1}$ and $\hat{e}_{r_2}$ are the unit vectors along the axes of the vertical legs with their origin at the centre of the structure.

We can compute $\hat{e}_{r_1}$ and $\hat{e}_{r_2}$ as follows:

$$\hat{e}_{r_1} = \frac{\vec{r_1}}{\|\vec{r_1}\|} \text{ and } \hat{e}_{r_2} = \frac{\vec{r_2}}{\|\vec{r_2}\|},$$

where $\vec{r_1}$ and $\vec{r_2}$ are the lengths of the springs after deformation measured from their attachment point to the location of the central hub, such that

$$\vec{r_1} = \sqrt{(x + l_1 \cos\alpha)^2 + z^2} \qquad \text{and} \qquad \vec{r_2} = \sqrt{(-l_2 \cos\alpha + x)^2 + (l_2 \sin\alpha + z)^2}.$$

where l_1 and l_2 are the length of the support legs.

The stiffnesses of the springs k_1 and k_2 are computed with the axial stiffness equation, such that

$$k_1 = \frac{EA}{l_1} \text{ and } k_2 = \frac{EA}{l_2}.$$

We consider $E = 210$ GPa as the elastic modulus for offshore structural steel and 1 m diameter for the legs of the v-frame (as specified in *D6.2 Transportation and Maintenance LiftWEC ULS Assessment* [14]). We then assume a v-frame height of $h = 40$ m and a leg to leg horizontal distance of $w = 60$ m (see for example *LW-WP06-AAG-N02-1x2 Effect of water depth on support structure of Config 2* [15]). This yields $l_1 = l_2 = 50$ m. The estimated stiffnesses are $k_1 = 3.14E9$ N/m and $k_2 = 3.14E9$ N/m. We note that these are high stiffnesses that might constrain the movement of the structure. Therefore, in the remaining of the report lower stiffnesses will be utilised to understand the effect of compliance in the structure and analyse the effect that compliant moorings or floating structures could have in the performance of LiftWEC.

6.2   FREE MOTION OF SUPPORT STRUCTURE

A free oscillation is imposed on the system for a duration of $1T_p$. A displacement of 1 m is applied in both x and z-directions. Two cases are presented. One where the spring stiffnesses are both $k = 3.14E9$ N/m (high stiffness) and another one, where both stiffnesses are reduced by three orders of magnitude, i.e. $k = 3.14E6$ N/m.

The effect of stiffness is clear in the natural frequency of the systems. Higher stiffnesses result in higher frequency oscillations, as shown in Figure 19a. In contrast, lower stiffnesses yield a lower natural frequency, as shown in Figure 19b. In terms of power output both cases are within 0.1% from each other and no significant difference between these two free-oscillating cases is observed.
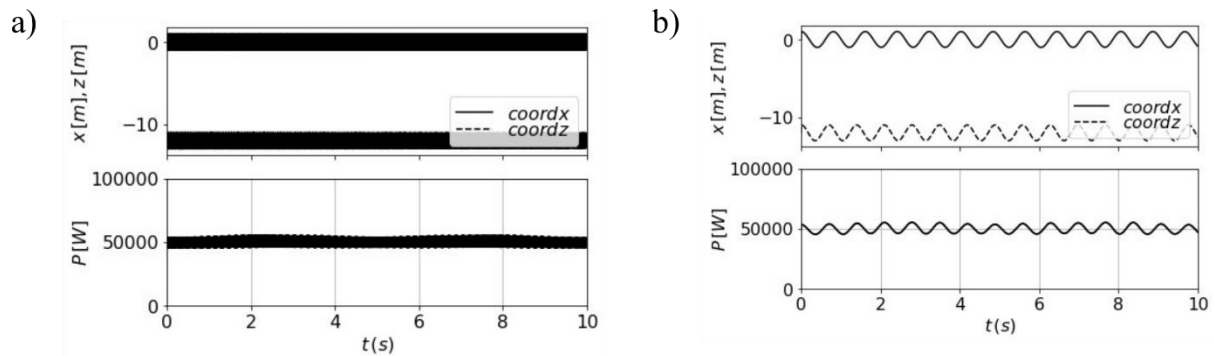
Figure 19 Free oscillation of structure in the x and z-directions and mean power output P_{av} for a cycle of rotation with wave parameters of $T_p = 10\ s, H_s = 3\ m$ and $\omega = 2\pi/T_p$. An initial displacement at the hub of 1 m is applied in both x and z-directions for a) high stiffness case ($k_1 = k_2 = 3.14E9\ N/m$) and b) low stiffness case ($k_1 = k_2 = 3.14E6\ N/m$).

6.3   FORCED MOTION OF SUPPORT STRUCTURE

In order to excite the structure with hydrodynamic forces, the radial forces are decomposed into the x and z- directions. A rotation cycle of the components of the radial force is shown in Figure 20, where F_{x_1} and F_{x_2} are the components of the radial forces of hydrofoil 1 and 2 in the horizontal axis, whilst F_{z_1} and F_{z_2} the components in the vertical direction. It is worth noting that the horizontal components lag the vertical components by approximately 90°.
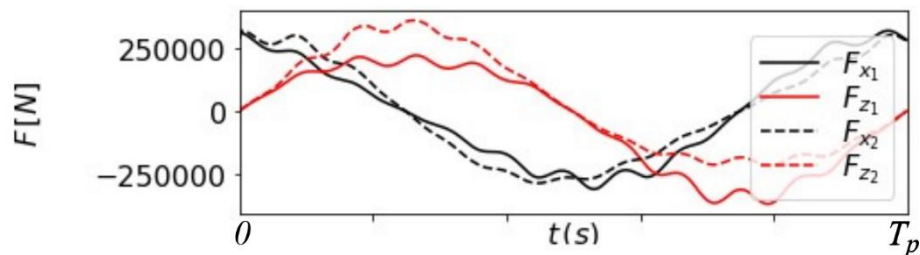

Figure 20 Radial forces in the x and z-directions applied to excite the support structure during 1Tp for the design tested conditions

Two cases are tested a) high stiffness ($k_1 = k_2 = 3.14E9$) and b) low stiffness ($k_1 = k_2 = 3.14E6$) to assess the effect of compliance in the power output. In these two scenarios compliance does not seem to be detrimental to performance in terms of average power output. The difference in P_{av} between the two cases is of 0.01%. The red line in the figures shows P_{av}.
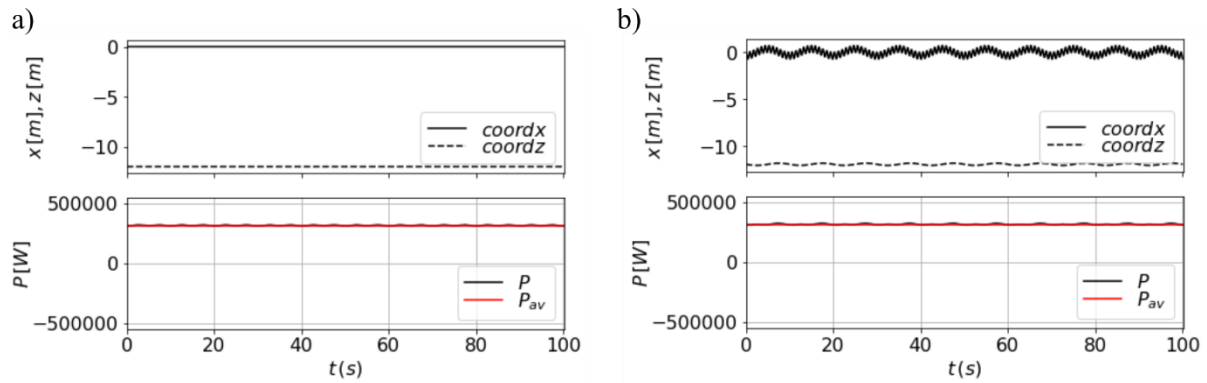

Figure 21 Structural response in the x and z-axes of the support structure for 10Tp, with a) high and b) low stiffness case. Both cases are excited by the radial force components in the horizontal and vertical axis from the two hydrofoils

To further analyse the effect of compliance Figure 22 presents further results of the change in average power output (ΔP_{av}) as a function of compliance in the structure. The reference to compute ΔP_{av} is P_{av} at $k_1 = k_2 = 3.14E9$.
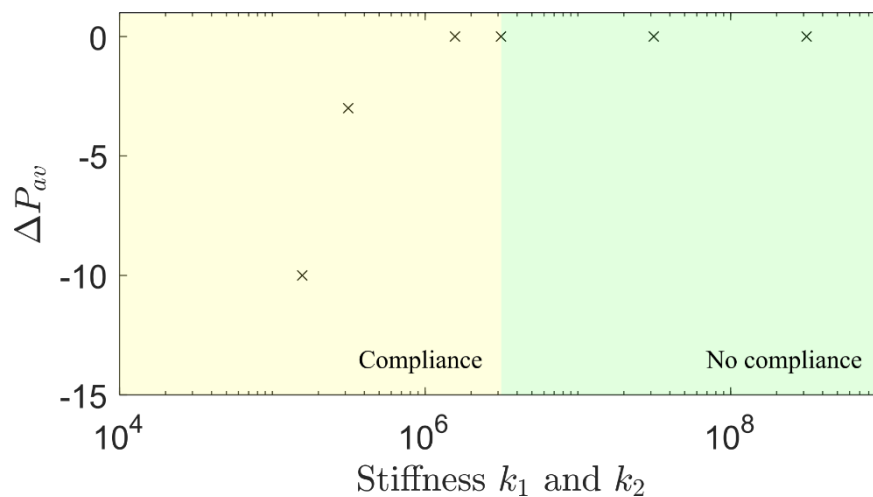

Figure 22 Change in average power output (P_{aav}) versus support structure stiffness k1 and k2

Results show that at high stiffness values, highlighted by green in the figure ($k_1 > 3.14E7, k_2 > 3.14E7$), i.e. no compliance or motion of the structure, the power production remains constant. A slight drop in average power occurs when the stiffness of the structure allows motion above 1 m (yellow region). We note, however, that motions over 1 m are not expected to be realistic within the range of commercial materials for the v-frame support structure. Hence, the impact of the dynamics of the structure in the power output of LiftWEC is expected to be minimal.

We note, however that motion of the v-frame could have an impact in the fatigue life of the structure, i.e. it could be possible that increasing the compliance decreases the structural penalty on the structure. This, however, is a topic of further research in the subsequent work package deliverables.

7 CONCLUSIONS

This report constitutes Deliverable 'D6.3 Structural Dynamic Model Development" of the LiftWEC project. For this study, the device was divided in three main structural subcomponents: 1) the foils, 2) the central shaft and 3) the support structure.

As part of this deliverable a full evaluation of structural dynamic characteristics of each subcomponent was performed, with emphasis given to scenarios that could amplify motions of the structure. As part of control strategies passive radial motion, angular velocity capping and passive support structure deformation was analysed.

Single hydrofoil compliance, where the compliance is on the hydrofoil that experiences a positive radial load, was found to be beneficial in terms of power extraction of the LiftWEC device. The compliance, however, would need to be implemented through springs or deformable elastic material that allows for the required passive deformation of one of the foils in a two-foil rotor system. Importantly, commercial materials such as steel or aluminium alloy do not provide the level of passive deformation to enhance power extraction due to simple compliance.

When the inertia of the rotor is considered, our results showed that simple compliance is still beneficial for power extraction. Hence, inertia is not detrimental for enhancing power extraction through radial motion. Finally, compliance in the support structure is not found to be detrimental within the range of motions expected for rigid materials in the marine environment.

Hence inertia and motion of the support structure are not detrimental for enhancing power through simple radial compliance. In particular, the system can operate safely and stay away from resonant behaviours over a wave period range between $6\,s < T_p < 14\,s$.

8 BIBLIOGRAPHY

[1]   S. S. Rao, Mechanical vibrations, Prentice Hall, 2010.

[2]   A. Arredondo-Galeana, W. Shi, G. Olbert, M. Scharft, A. Ermakov, J. V. Ringwood and F. Brennan, "A methodology for the structural desing of LiftWEC: A wave-bladed cyclorotor," in *European Wave and Tidal Energy Conference (EWTEC)*, Plymouth, 2021.

[3]   N. Scharmann, Ocean energy conversion systems: The wave hydro-mechanical rotary energy converter, Hamburgh: PhD Thesis, 2014.

[4]   J. V. Wehausen and E. V. Laitone, Surface waves, Berlin, Heidelberg: Springer, 1960.

[5] S. J. T. M. T. Siegel, "Deep ocean wave energy conversion using a cycloidal turbine," *Applied Ocean Research,* vol. 33, no. 2, pp. 110-119, 2011.

[6] A. Ermakov and J. V. Ringwood, "A control-oriented analytical model for a cylorotor wave energy device with n-hydrofoils," *Jounral of Ocean Engineering and Marine Energy,* vol. 7, no. 2, pp. 201-210, 2021.

[7] M. Accensi and C. Maisondieu, "HOMERE. Ifremer - Laboratoire Comportement des Structures en Mer.," 2015.

[8] A. M. Cornet, "A global wave energy resource assessment," in *The Eighteenth International Offshore and Polar Engineering Conference*, Vancouver, Canada, 2008.

[9] K. Ramesh, J. Murua and A. Gopalarathnam, "Limit-cycle oscillations in unsteady flows dominated by intermittent leading-edge vortex shedding," *Journal of Fluids and Structures,* vol. 55, pp. 84-105, 2015.

[10] B. H. K. Lee, S. J. Price and Y. S. Wong, "Nonlinear aerolastic analysis of airfoils: bifurcation and chaos," *Progress in Aerospace Sciences,* no. 35, pp. 205-334, 1999.

[11] A. Arredondo-Galeana, W. Shi and F. Brennan, "LiftWEC: D6.1 Extreme Event LiftWEC ULS Assessment," 2020.

[12] K. a. B. F. Sunday, "A review of offshore wind monopiles structural design achievements and challenges," *Ocean Engineering,* vol. 235, 2021.

[13] A. Friedman, "NonlinearAnimation," 12 04 2021. [Online]. Available: https://github.com/apf99/NonlinearAnimation.

[14] A. Arredondo-Galeana, N. Clave, R. Pascal, S. Weichao, F. Brennan and P. Lamont-Kane, "LiftWEC: D6.2 Transportation and Maintenance LiftWEC ULS Assessment," LiftWEC, 2020.

[15] A. Arredondo-Galeana, *LW-WP06-AAG-N02-1x2 Effect of water depth on support structure of Config 2,* LiftWEC, 2021.

[16] P. Lamont-Kane, M. Folley, C. Frost and T. Whittaker, "A methodology for the structural design of LiftWEC: A wave-bladed cycloidal rotor," in *The 14th European Wave and Tidal Energy Conference, EWTEC 2021*, Plymouth, 2021.

9 APPENDIX 1 – VALIDATION OF NUMERICAL CODE

This appendix shows the hydrodynamic model validation utilised in this report. In this deliverable, the two-dimensional numerical simulations force data from Scharmann [3] is utilised here to validate, qualitatively, the outputs of the hydrodynamic model.

The numerical methodology from Scharmann was developed in the commercial solver Ansys CFX and was validated with experimental tests of a laboratory-scale two-bladed cyclorotor device. He then extended his numerical methodology to a large-scale device, and compared the results computed with Ansys CFX and OpenFoam. Here, because we are interested in the structural penalty of a large-scale rotor ($r \geq 6$ m, $c = 4$ m), we utilise his results for a large-scale device computed in Ansys CFX, which are valid under the assumption of two-dimensional flow.

The wave design parameters used by Scharmann [3] are $T_p = 8\,s$ and $H = 3$ m. We note that these parameters are different to our wave design parameters specified in Table 1. The remainder of the rotor parameters are $r = 10$ m and $c = 4$ m. The submergence depth (μ), phase difference ($\Delta\varphi$) and water depth (h) are not specified by Scharmann. Here, we make estimates of these parameters. We note that because $H = 3$ m, in order for the hydrofoils to remain under the through of the wave, the minimum submergence should be $\mu > 3$ m. Hence, we set $\mu = 4$ m, where $\mu \pm 1$ m does not change the model outputs significantly. Then $h =$50 m, because we consider intermediate water depths, and deeper water depths ($h > 50$ m) do not change the trends in the modelled results. Whilst $\Delta\varphi = 90°$ is chosen for hydrofoil 1, to set the rotor to the optimum phase [2].

Figure 23 shows the comparison of the hydrodynamic model outputs to the results from Scharmann [3]. The figure shows F_T (Figure 23a) and F_R (Figure 23b) for one normalised period of revolution t/T_p. Results are shown for the two hydrofoils. The model outputs are shown with solid and dotted black lines for hydrofoil 1 and 2, respectively. Scharmann's results are plotted with solid and dotted red lines, for hydrofoils 1 and 2, respectively. We note that F_T is considered positive pointing outwards of the chord of the foil, whilst F_R is defined positive pointing along the same direction in both hydrofoils.

In Figure 23, a good match (within 2%) between the predicted and Scharmann's F_{T2} is seen, whilst the predicted F_{T1} shows a similar trend to Scharmann's curve but has a different peak magnitude. The maximum amplitude of this peak is about a third of that predicted by our current model. Here, the subindices refer to hydrofoil 1 and hydrofoil 2. Inb shows similar trends for F_R, in the two hydrofoils, between Scharmann's results and the current model. With the current model over predicting the maximum amplitude of the loads by about 25%. Discrepancies could be due to unsteady effects that are not accounted for in the hydrodynamic model. The model also does not consider forces on the hydrofoil due to radiated waves, which will have some impact, but these will depend on the width of the hydrofoil *[6, 16]*. However, we recall that the purpose of this report is to develop an initial structural dynamics assessment of LiftWEC. As such, future refinements to the hydrodynamic model can be included.
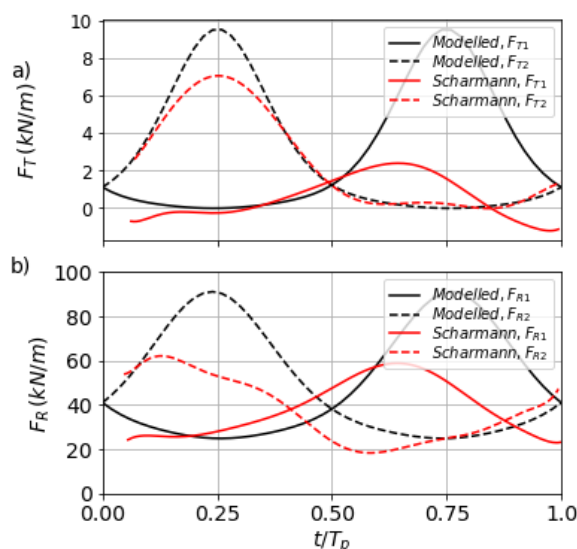
Figure 23 Tangential (F_T) and b) radial forces (F_R) computed for hydrofoil 1 and 2 (solid and dotted black lines) of a LiftWEC rotor in one period of rotation (t/T_p), compared to results of two-dimensional numerical simulations by Scharmann [3].

10   APPENDIX 2 - STATE-SPACE NOTATION

It is useful to illustrate the steps to solve the equations of motion also in state-space notation. We chose equation 1 (radial motion), to illustrate the solution procedure, as follows:

1) First, we re-arrange equation 1 as shown in the right column and define auxiliary variables x and $\dot{x}$

$$\ddot{h} = (F_R - k_h h)/m \qquad \text{Eq. (1)}$$
$$x = \dot{h}$$
$$\dot{x} = \ddot{h}$$

2) Then, we define the state-space vectors as follows

$$\begin{Bmatrix} \dot{h} \\ \dot{x} \end{Bmatrix} = \begin{Bmatrix} x \\ (F_R - k_h h)/m \end{Bmatrix}$$

3) We group the state-space vector into a single expression, such that

$$\{\dot{\vec{y}}\} = \{\vec{F}\}$$

4) we approximate numerically the term on the left hand side, such that

$$\left\{ \frac{\vec{y}_{t+1} - \vec{y}_t}{\Delta t} \right\} = \{\vec{F}\}$$

5) Rearranging yields

$$\{\vec{y}_{t+1}\} = \{\vec{y}_t + \Delta t\, \vec{F}\}$$

6) Finally, we solve the state-space vector

$$\{\vec{y}_t\} = \begin{Bmatrix} h \\ \dot{h} \end{Bmatrix} = \begin{Bmatrix} heaving\ displacement \\ heaving\ velocity \end{Bmatrix}$$

Table 4 Steps in state-space notation to solve Equation 1, which corresponds to the radial motion of the foils

11 APPENDIX 3 - LAGRANGE EQUATIONS

The equations of motion utilised in this work are derived through Lagrange equation, which states that

$$\frac{d}{dt}\left(\frac{\partial T}{\partial \dot{q}}\right) - \left(\frac{\partial T}{\partial q}\right) + \left(\frac{\partial U}{\partial \dot{q}}\right) = Q,$$

where T and U are the kinetic and the potential energy of the system, q is the vector containing the generalised coordinates of the system and Q are the forces that excite the system. We recall that for a linear spring, such as the ones utilised in this study, the potential energy is

$$U = \int_0^q F d\mathbf{q},$$

where $F = k\mathbf{q}$, for a linear spring, and k is the stiffness of the spring. And the kinetic energy is

$$T = \frac{1}{2}mv^2,$$

where m and v are the mass and the velocity of the system, respectively.